Top Catal (2015) 58:545–558
DOI 10.1007/s11244-015-0396-7

Nucleation, Growth, and Robust Synthesis of SPP Zeolite: Effect of Ethanol, Sodium, and Potassium

Garrett R. Swindlehurst[1] · Prashant Kumar[1] · Dandan Xu[1] · Saeed M. Alhassan[2] · K. Andre Mkhoyan[1] · Michael Tsapatsis[1]

Published online: 3 April 2015

Abstract Self-pillared pentasil (SPP) zeolite is a hierarchically-structured zeolite comprised of single-unit cell thick MFI nanosheets arranged in a "house of cards" structure. The nucleation and growth of SPP proceeds through three phases involving the evolution of precursor amorphous nanoparticles to MFI nanosheets and then rotational intergrowth of sheets to produce the SPP morphology. This paper expands upon an earlier report to extend understanding of nucleation and growth events throughout the entire preparation process, from hydrolysis of the silica source to high conversion to crystals. Common aspects with the extensively investigated clear-sol silicalite-1 system are identified. Evaporation of co-solvent ethanol was found to accelerate the crystallization significantly. Furthermore, robust synthesis of SPP with high density of well-developed single-unit cell domains has been achieved with addition of potassium and sodium to the synthesis sols.

Keywords Hierarchical · Zeolites · Intergrowth · Nucleation and growth · SPP · Robust

Electronic supplementary material The online version of this article (doi:10.1007/s11244-015-0396-7) contains supplementary material, which is available to authorized users.

✉ Michael Tsapatsis
tsapatsis@umn.edu

[1] Department of Chemical Engineering and Materials Science, University of Minnesota, 421 Washington Ave SE, Minneapolis, MN 55455, USA

[2] Department of Chemical Engineering, Petroleum Institute, Abu Dhabi, United Arab Emirates

1 Introduction

It is our great pleasure to provide this contribution to the special issue honoring Professor Mark E. Davis. It builds on goals and approaches to understand and control growth of zeolite nanostructures introduced early on by the Davis' laboratory [1–6]. In the last 20 years, professor Davis's interest, critical suggestions and continuous encouragement have been an inspiration in our efforts to shrink zeolite crystal size to the single-unit-cell level [7].

Hierarchical zeolites are crystalline silicates or aluminosilicates containing pores with regular dimension in the micropore (0.5–2 nm) and mesopore (2–50 nm) range [8]. The microporous crystallinity of the morphology confers the familiar interesting properties of "bulk" zeolites to interacting chemical species, primarily resulting from three-dimensional confinement in pores at the molecular scale [9–11]. As the thickness of the microporous zeolite domains between mesopores decreases, the characteristic length scales for micropore diffusion approach the size of a single unit cell of the corresponding zeolite (e.g. 1–5 nm) and the externally-accessible surface area per unit mass is maximized [12, 13]. This dramatic change in physical dimensions important to reaction and adsorption processes lends this class of materials markedly different behavior from the corresponding bulk zeolites in certain applications [14–16].

In the past several years, two major techniques have been used for the preparation of hierarchical zeolites. Use of various meso-structuring materials, such as mesopore templating molecules [14, 17, 18], colloidal crystals [19–21], and "pillaring" of two-dimensional layered zeolites to impart three-dimensional stability [22] have been explored to generate mesopores with regular form and structure within zeolites. Subtraction of zeolitic material with

techniques such as desilication [8, 23, 24] or dealumination [25, 26] has also been successful at mesopore direction, albeit with less control over both shape and regularity. In both approaches, considerable additional steps have to be added to the synthesis processes compared to bulk zeolite preparation procedures. This addition of technically challenging and/or time consuming steps adds significant cost to the process, likely rendering the large-scale industrial synthesis of these materials economically unfeasible. Recently, our group proposed a new synthesis strategy for generating hierarchical zeolites with regular mesopores and microporous domains down to single-unit cell thickness [27]. The morphology, termed self-pillared pentasil (SPP) zeolite, results from the intergrowth of two different zeolite frameworks in a "bottom–up" synthesis approach of a hierarchical zeolite, as opposed to the "top–down" approaches previously reported. In SPP, a lower-symmetry framework (MFI) grows as two-dimensional nanosheets, which are then connected in a "house of cards" structure by intersection through a one-dimensional zeolite crystal of higher symmetry (MEL) and compatible silica connectivity. The regular and repeated intergrowth of these two zeolite frameworks with single-unit cell dimensions gives rise to hierarchically-structured zeolite nanoparticles reducing diffusion limitations for species involved in reactions at micropore active sites [27]. This morphology is accessible through a single-step hydrothermal synthesis using only carefully tailored composition and temperature, and without the aid of any additional templating agents beyond the standard micropore structure directing agent employed in many zeolite syntheses. The one-step synthesis of hierarchical zeolite formed by the intergrowth of two zeolite crystal structures has been explored in other systems, including MFI with diquarternary-C5 as a structure directing agent [28] and FAU/EMT [29, 30], and may be observable in other systems such as ETS-4/ETS-10 [31], CAN/SOD [32], and CHA [33]. The approach shows promise for the preparation of novel hierarchical zeolites with reduced diffusion limitations; however, only the SPP morphology has thus far been observed to contain zeolite nanosheets of single unit cell thickness.

Previously, it was demonstrated with combination of small-angle X-ray scattering (SAXS) and transmission electron microscopy (TEM) studies that the nucleation and growth of the SPP morphology occurs in three distinct phases (Fig. 1) [34]. During the first phase of hydrothermal treatment, precursor amorphous nanoparticles of spheroid form and size 2–4 nm occur in high population in the ethanol/water solvent mixture. Phase 2 occurs after a certain time (8.5 h at 120 °C), wherein a second population of larger crystalline nanoparticles with size 10–50 nm appears in small amounts. High-resolution TEM (HRTEM) imaging of the sols revealed these to be two-dimensional "nanosheets" of MFI, as evidenced by observation of the straight-channel micropores along the (010) axis. With further heating to Phase 3, these nanoplates grow further along the (100) and (001) axes and rotationally-intergrow to form the SPP structure. The combination of SAXS and TEM imaging allowed confirmation of the "bottom-up" growth mechanism of the hierarchical structure first proposed by Zhang et al. based on symmetry arguments and characterization of fully-grown SPP crystals [27].

In this paper, two aspects related to the synthesis and characterization of SPP are reported. First, the combination SAXS and TEM investigation of the nucleation and growth dynamics of the morphology from Xu et al. [34] are extended to characterize the sol components at earlier and later stages of synthesis. An investigation into accelerating crystallization via the evaporation of co-solvent ethanol is also presented. Second, the addition of alkali metal cations to synthesis sols which promotes robust crystallization of SPP composed of single-unit cell thick zeolite nanosheets intergrown at right angles throughout the nanoparticles is investigated with TEM, XRD, and gas physisorption. Together, these reports bring new insight regarding the robust and reproducible synthesis of SPP and may aid efforts to scale up the production of this hierarchical zeolite for industrial application.

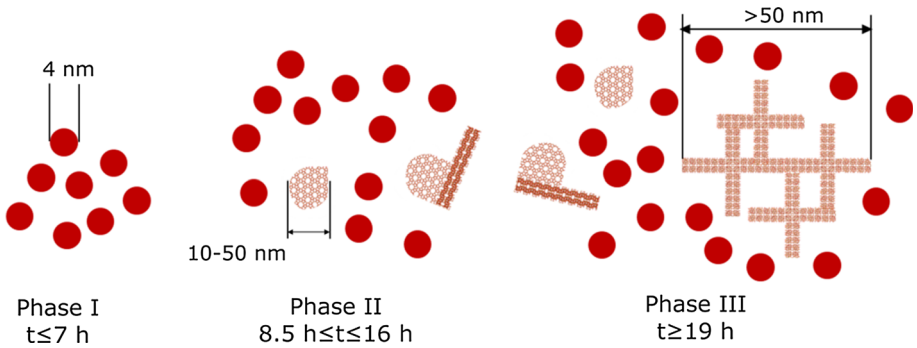

Fig. 1 Schematic of the originally-proposed three phases of SPP nucleation and growth. Reprinted from [34] with permission from authors

2 Experimental

2.1 Synthesis

The silica sols for SPP synthesis were prepared with the composition 10 SiO_2:3 SDAOH:x MOH:100 H_2O:40 EtOH, where SDA (structure-directing agent) was tetrabutylphosphonium hydroxide (TBPOH, 40 % by weight, TCI America), M was either K or Na, and x ranged from 0 to 0.5. The SDA solution was firstly added drop-wise into tetraethylorthosilicate (TEOS, 98 %, Sigma-Aldrich) with vigorous stirring until the system turns clear. Then ultrapure water (18 MΩ-cm, Milli-Q, Millipore) with or without dissolved KOH or NaOH (Sigma-Aldrich) was added into the clear system at room temperature and stirred to yield the hydrolyzed sol. To evaporate ethanol following room temperature hydrolysis, samples were weighed and added to a round-bottom flask, then spun on a Rotovapor (Büchi) in a water bath at 60 °C for 10 min. The samples were then subject to vacuum and de-pressurized to just above the boiling point of the sol with rapid rotation, removed, and subsequently weighed. Evaporation was considered complete when sol mass equivalent to the calculated mass fraction of ethanol in the sol composition was lost to evaporation. The clear sols from room temperature hydrolysis or ethanol evaporation steps were sealed with Teflon tape and further hydrolyzed at 80 °C in a Teflon bottle with continuous stirring. After 48 h, the clear sol (18.3 g) was quickly transferred to a preheated 45 mL Teflon-lined stainless steel autoclave at 70 °C, sealed and heated for 3–48 h in a pre-heated oven at 115 or 120 °C. After heating, the final sols were quenched in water and then collected for further characterizations. To obtain powdered samples for adsorption, electron microscopy, and diffraction studies, the fully-crystallized sols were washed repeatedly by centrifugation with redispersion in ultrapure water until pH 8. Samples were taken for TEM study after the final redispersion, and then the suspensions were centrifuged once more and dried in a vacuum oven for 24 h at 70 °C. Samples were then ground to a powder and then calcined to remove SDA at 550 °C for 12 h, after which the final powder was obtained.

2.2 Characterization

SAXSess (Anton-Parr) was used to obtain small-angle X-ray scattering patterns from the sols after hydrothermal treatment. The sols were placed into a vacuum-tight 1 mm quartz capillary. All measurements were carried out at room temperature (25 °C). The scattering vector q was calculated from the scattering angle 2θ through $q = 4\pi\lambda^{-1}\sin\theta$, with $\lambda = 0.154$ nm for the Cu K-α radiation source. Scattering from an equivalent ultrapure water or 10:4 water–ethanol mixture was used as a background pattern and subtracted from all sample scattering patterns. Patterns were then de-smeared from the beam profile and fitted using the GIFT program. Pair distance distribution functions (PDDF) were obtained by indirect Fourier transformation (IFT) or generalized indirect Fourier transform (GIFT) of the fitted data [35].

The as-synthesized synthesis sols were diluted 1:10 by volume into ultrapure water and used for TEM samples. TEM samples were also prepared from centrifuged-washed samples as described above. Calcined powders were vigorously sonicated in ethanol to disperse particles and then used to prepare TEM samples. Specimens were prepared by placing droplets of the diluted sol onto a copper-backed sample grid coated with ultra-thin and holey carbon films (Ted Pella Inc.). The specimens were dried at room temperature in air. TEM imaging was performed on a FEI Tecnai G2 F30 (S)TEM with TWIN pole piece, a Schottky field-emission electron gun operating at 300 kV and equipped with a Gatan 4 k × 4 k Ultrascan CCD. HR-TEM imaging was performed in an FEI Tecnai G2 F30 (S)TEM with S-TWIN pole piece and a Schottky field-emission electron gun operating at 300 kV [36].

Argon (87.3 K) adsorption was performed using a commercially available automatic manometric sorption analyzer (Quantachrome Instruments Autosorb iQ MP). Prior to adsorption measurements, the samples were outgassed at 573 K for 16 h under turbomolecular pump vacuum. Full micro and mesopore size distributions were calculated from the argon isotherms using the argon on zeolites/silica cylindrical pore adsorption branch method [37]. X-ray diffraction (XRD) patterns were acquired using a X'Pert PRO MPD X-ray diffractometer (PANalytical) equipped with a Co source.

3 Results and Discussion

3.1 Nucleation and Growth of Pure-Silica SPP

Previously, our group reported the robustness of SPP morphology formation in pentasil zeolites crystallized at 115 and 120 °C from sols of hydrolyzed tetraethylorthosilicate (TEOS) with final composition 10 SiO_2: xTBPOH:yH_2O:40 EtOH, where x ranges from 2 to 4 and y ranges from 70 to 200 [27]. The optimal composition for a morphology showing uniform crystal size and highest abundance of pentasil nanosheets intergrown at right angles was determined to be x = 3 and y = 100, with crystallization taking place at 120 °C for 40 to 48 h [34]. Further investigations revealed that the temperature range for obtaining the best morphology and high conversion of silica to zeolite crystals was rather flexible, with good

crystals obtained by 40 h at 115 °C but with rather low conversion, and conversion increasing from 40 to 48 h. It was also found that freshly-opened TBPOH solutions yielded the best morphology (results not shown).

To investigate the crystallization process further, small-angle X-ray (SAXS) patterns were obtained on sols with the optimal composition above and subject to variations on heat treatment (Fig. 2). SAXS is particularly suited to the analysis of precursor sols to zeolites, as a single profile can yield information about the sizes and relative populations of amorphous and crystalline particles that evolve during the crystallization process [34, 38, 39]. Furthermore, as larger lengths between scattering centers scatter much more intensely than smaller lengths, the first crystals that appear in the sol can be detected easily among the much more numerous precursor particles, as long as the crystals are significantly larger [40, 41]. The first extension of the previous synthesis study was to investigate the nanoparticle populations of the sol prior to hydrothermal treatment. The first step of SPP synthesis is combination of the pure-chemical precursors to the sol at room temperature. Upon mixing of TEOS, 40 % TBPOH aqueous solution, and excess water at room temperature, hydrolysis of the silica source produces silicic acid and silica oligomers until a critical concentration is reached, resulting in silica polymerization and formation of small amorphous silica nanoparticles [38, 42]. Previous TEM results indicate that the nanoparticles are roughly spherical throughout hydrothermal treatment [34]. After the initial mixing, sols hydrolyzed at room temperature display a global maximum in the SAXS profile (black curve) for $q > 0$. Since there is no global maximum in the X-ray scattering form factor for spheroids, this maximum indicates that the dilute sol approximation to scattering, in which only form factor significantly contributes to the scattering pattern, must not apply in this system.

In SAXS, scattering patterns result from the sum of interactions between incident X-rays and electron density fluctuations about the mean in a sample. The scattering intensity from a continuous electron density distribution is given by Eq. 1,

$$I(q) = \langle |E_s(q)|^2 \rangle = \langle \int_v \Delta\tilde{\rho}^2(\mathbf{r}) e^{-iqr} d\mathbf{r} \rangle = \int_0^\infty 4\pi r^2(r) \frac{\sin(qr)}{qr} dr \quad (1)$$

where q is the scattering vector given from the Bragg equation as $q = (4\pi \sin(\theta/2))/\lambda$, $\Delta\tilde{\rho}^2(\boldsymbol{r})$ is the spatial autocorrelation of electron density fluctuations about the mean density, and $p(r) = r^2\gamma(r)$ is the pair-distance distribtion function (PDDF) of the scattering lengths r in the system [43]. In a sol with high volume fraction of particles, there can exist fluctuations of density $\Delta\tilde{\rho}^2(\boldsymbol{r})$ below the average density of the sample [44], where the average density is between that of colloidal silica particles and the water/ethanol mixed solvent. If the structure factor effects which account for interparticle scattering are not removed by modeling, $p(r)$ generated from an inverse Fourier transform of the scattering data does not represent the autocorrelation function $\gamma(r)$ of individual particles and thereby their actual dimensions, but rather the form and structure of the sol combined.

As a result, IFT analysis on SPP sols after the first hydrolysis step shows local minima at negative intensities, indicative of strong structure in the sol and areas of the sample with electron density below the sample average (Fig. 2). Performing a Generalized Indirect Fourier Transform (GIFT) analysis on this data allows separation of the structure and form factor contributions to the scattering pattern based on a repulsive polydisperse hard sphere model for the nanoparticles [35]. The structure factor S(q) resulting from GIFT analysis on the sol prior to heat treatment is characteristic for the radial distribution function of concentrated fluid spheres (Fig. S1, Supplementary Information). The hard sphere model fit to the data indicates spheres with radius 1.1 nm and polydispersity of 1.03 comprise the sol. This structured, concentrated sol of amorphous silica nanoparticles with radius of about 1 nm exists prior to any heat treatment, similar to clear-sol silicalite-1 systems at similar compositions [41]. Dynamic light scattering has also been used previously on sols with TBPOH at similar concentrations to confirm the initial presence of amorphous silica colloids with diameter near 2 nm following hydrolysis [45]. Si^{29}-NMR studies of the silicalite-1 system have shown that nanoparticles formed after initial TEOS hydrolysis are very loosely-connected and contain many Q_2 and Q_3 silicon atoms [46], and so the sol structure in the similar SPP system is most likely imparted by a combination of high particle density and high negative surface charge. Following high-temperature hydrolysis at 80 °C for 24 h, the global maximum at q = 2.5/nm becomes a shoulder in the SAXS pattern and a second shoulder emerges. The two shoulders near q = 1 and 2.5/nm are resolved by IFT analysis, and the PDDF indicates a larger nanoparticle population with radius near 3 nm in the structured sol has been formed. From this point forward in the synthesis, the heterogeneity of particle populations in the sol precludes the selection of an appropriate model for the structure factor, therefore the results of the IFT analysis yield PDDF exhibiting both structure and form factor effects. In our previous model for SPP nucleation and

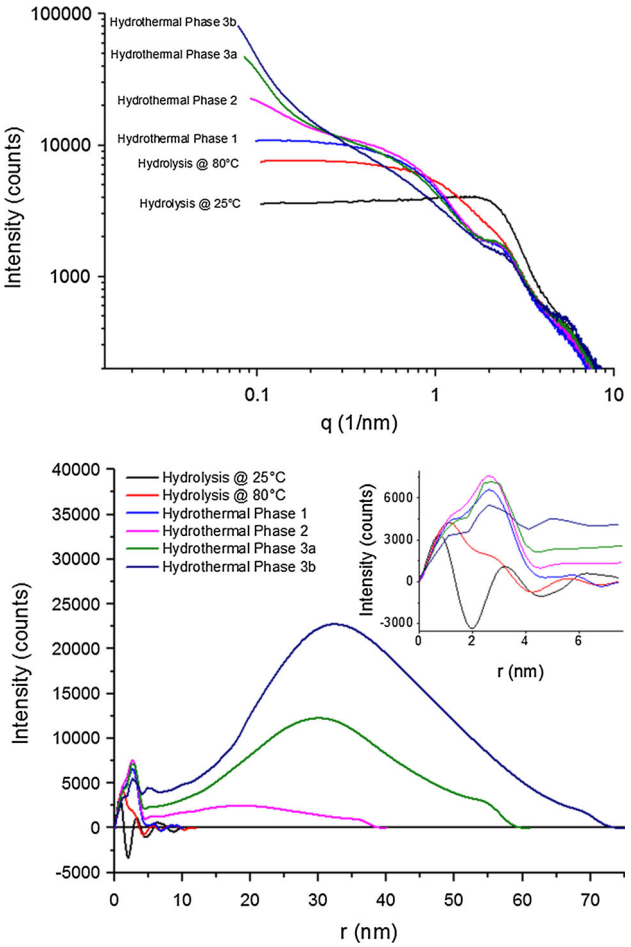

Fig. 2 Small angle X-ray scattering (SAXS) patterns (*top*) and resulting pair-distance distribution (PDDF) functions (*bottom*) from SPP sols with composition 10 SiO_2:3 TBPOH:100 H_2O:40 EtOH at various stages of synthesis. *Black*, hydrolysis @ 25 °C; *red*, hydrolysis @ 80 °C; *blue*, hydrothermal Phase 1 of growth; *magenta*, hydrothermal Phase 2; *green*, hydrothermal Phase 3a; *purple*, hydrothermal Phase 3b

growth, the presence of a single 4 nm amorphous precursor particle population was proposed based on the SAXS patterns and PDDF obtained after various hydrothermal treatment times, and was believed to agree with previous results on the silicalite-1 system studied by Davis and coworkers [39]. The updated study of the hydrolysis period demonstrates that the nanoparticle populations in the SPP system more closely resemble the concentrated silicalite-1 sols of composition 25 SiO_2:9 TPAOH:400 H_2O studied by Aerts et al [41]. In the more concentrated silicalite-1 sol, two populations with size 2 and 6 nm appear upon heating. The larger, higher-connected particles with $Q_{average} = 3.4$ have been proposed to be the primary participants in silicalite-1 crystal growth by aggregation. Their role in the SPP system, which lacks evidence of aggregation is unclear [34], but it is possible that they serve as nuclei for the single-unit cell thick nanoplates of MFI observed after several hours of hydrothermal treatment.

In our previous investigation, the evolution of SPP during hydrothermal synthesis treatment was broken down into three main phases based on the silica morphologies observed in the sol. After the additional precursor nanoparticle population was identified, a closer investigation of the phases of growth during hydrothermal treatment was conducted. During Phase 1 of the hydrothermal treatment at 115 °C, the first shoulder in the SAXS profile at q = 1/nm increases in intensity. The corresponding PDDF shows that the smaller nanoparticle population slightly increases in diameter while the larger nanoparticle population increases in number compared with samples heated at 80 °C. The scattering intensity from both precursor nanoparticle populations reaches a peak at Phase 2 of the synthesis. At this phase, intense low-angle scattering below q = 0.3/nm begins to appear in the system, indicating the nucleation of single-unit cell thick sheets of pentasil zeolite has occurred [34]. IFT analysis suggests that scattering lengths *r* in the system at Phase 2 are as large as 40 nm. As previously mentioned, a significant deviation between the SPP and silicalite-1 systems occurs at this stage of early crystal formation, as there is no evidence of aggregation of pre-crystalline or crystalline nanoparticles to yield larger crystals in the SPP system [34]. The continued increase in low-angle scattering intensity with further heat treatment leads to the formation of rotationally-intergrown SPP material in Phase 3 as previously observed. The largest scattering dimension observable has been increased compared to the previous study due to higher resolution of the SAXS instrument achieved by better alignment in the current study, which allowed us to obtain reliable data from lower scattering angles. The maximum dimension observable from SAXS agrees with the maximum particle size observable in TEM of 60–70 nm (Fig. S2, Supplementary Information). Another change in the SAXS patterns can be observed with 40+ h duration of hydrothermal treatment, in which the shoulder at q = 1/nm significantly decreases in intensity. To account for this difference in scattering, Phase 3 has been divided into Phase 3a and Phase 3b as an update to the previously proposed model. The decrease in the intensity of the first shoulder in the Phase 3b scattering profile and resultant PDDF indicates a decrease of the amorphous nanoparticle populations in the sol. The apparent density of amorphous precursor particles on TEM grids at Phase 3b of growth is significantly lower than Phase 3a, even though crystal size itself is not much changed between these phases at around 60 nm. The reduction in number of amorphous silica particles is therefore best attributed to an increase in the number of SPP crystals present in the sol. Precursor particle consumption with increased conversion

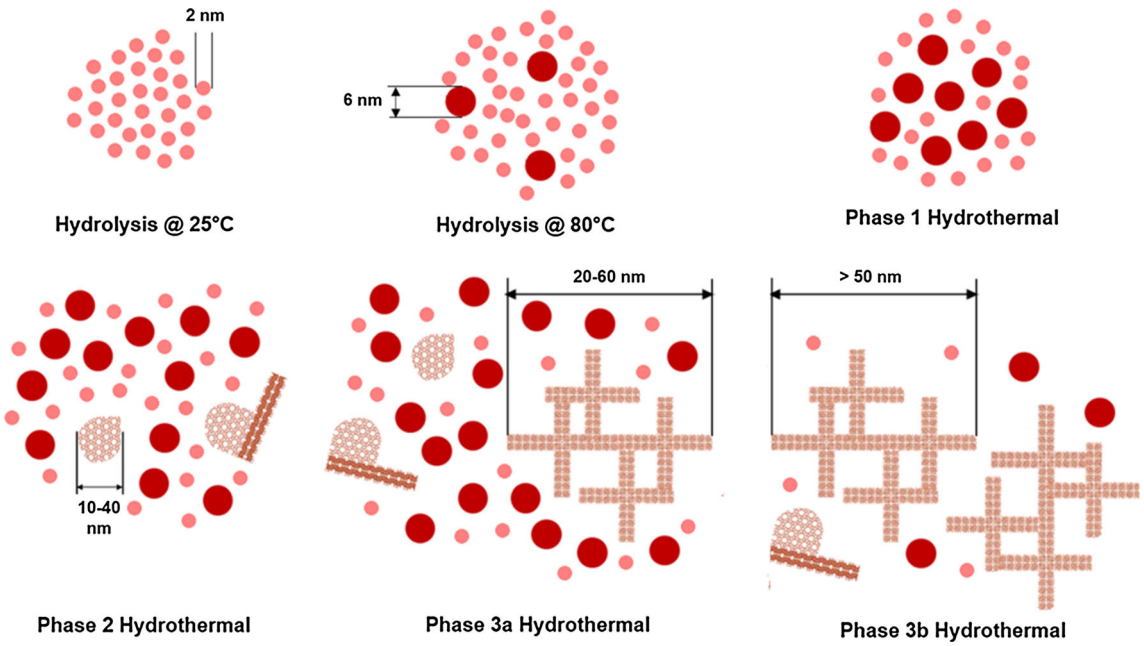

Fig. 3 Updated schematic of SPP nucleation and growth model from initial hydrolysis to high crystal conversion

to crystalline zeolite is also a feature of late-stage hydrothermal crystal growth also observed in the silicalite-1 system [41, 47]. The first Bragg peaks of SPP become observable between q = 5–6/nm at this stage where SPP first forms at significant density, and suggests that the number of crystalline particles is increased during Phase 3b. The detailed IFT analysis of SAXS patterns resulting from SPP precursor sols from the beginning of hydrolysis throughout hydrothermal treatment reveals that the evolution of nanoparticles and crystals is similar to the extensively-investigated silicalite-1 system in many respects. A scheme of the updated model of nucleation and growth including pre-hydrothermal synthesis steps—and later-stage crystallization is shown in Fig. 3.

Following the extension of the nucleation and growth model to cover the entire synthesis process, kinetic studies similar to previously reported results [34] using SAXS analysis were conducted to further clarify the time to onset of observed phases of nucleation and growth. Figure 4 shows SAXS profiles and corresponding PDDF from sols with increasing amounts of hydrothermal synthesis time at 115 °C. Phase 1 of growth, in which only amorphous precursor nanoparticles are present, lasts until 18 h. Between 18 and 24 h, the first crystalline pentasil nanoplates appear in the sol, and this Phase 2 lasts until 27 h. By 30 h at Phase 3a, these plates have converted to crystals first showing the rotationally-intergrown SPP morphology, but silica conversion to crystals is low, and precursor nanoparticle concentrations remain roughly the same as the

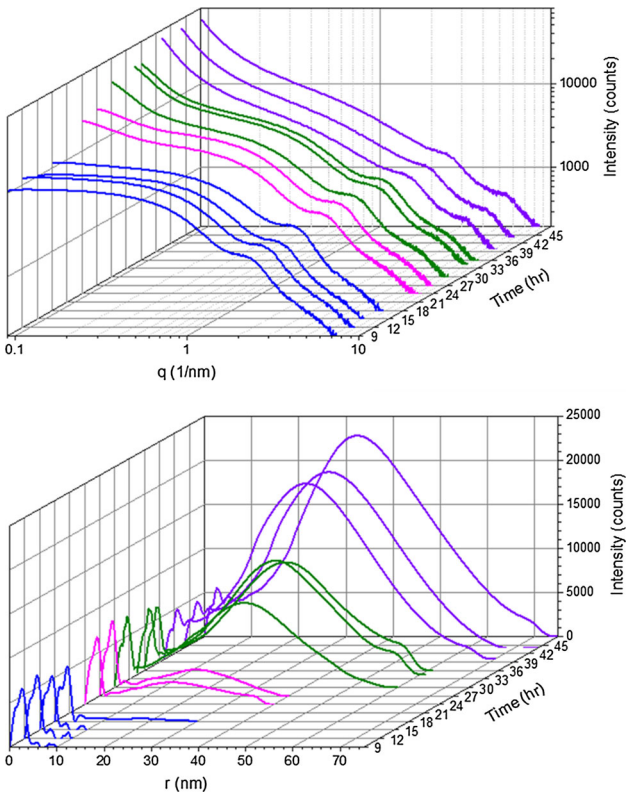

Fig. 4 Time-resolved SAXS patterns (*top*) and corresponding PDDF (*bottom*) from sols subject to 9, 12, 15, 18, 24, 27, 30, 34.5, 36, 40, 44, and 48 h of hydrothermal synthesis time at 115 °C. *Blue*, hydrothermal Phase 1 of growth; *magenta*, hydrothermal Phase 2; *green*, hydrothermal Phase 3a; *purple*, hydrothermal Phase 3b

earliest stages of growth. However, by 40 h at Phase 3b, low-angle scattering nearly doubles, the population of nanoparticles is significantly reduced, and the first Bragg reflections of the crystalline intergrown particles are observed, indicating the conversion of precursor nanoparticles to SPP crystals has occurred. The changes in SAXS patterns between different Phases of growth at 115 °C are not smooth, but show evidence of relatively rapid transitions between the different phases. In cases of Phase 2 and Phase 3a, profiles remain virtually unchanged over 3 or 6 h of hydrothermal synthesis time, respectively, and then show a marked shift to the next phase within a 3 h sampling window. These types of rapid shifts in silica distribution between soluble species, precursor particles, and crystals have also been demonstrated in the silicalite-1 system with various techniques [41, 48]. The primary difference between these data and those previously published by us was the age of the TBPOH solutions used in preparation of the sols. Repeating the same study at the previously-used temperature of 120 °C and with special care to use fresh TBPOH solutions yields SAXS patterns demonstrating the same rapid transitions between growth phases, as opposed to smooth transitions previously observed (Fig. S3, Supplementary Information). There was a slight increase in the rate of progression through the phases of growth with elevated temperature. Phase 2 and Phase 3 both arrived 3 h earlier than at 115 °C, but overall, the use of freshest TBPOH slowed down the synthesis by about a factor of two. Interestingly, Phase 3a of the proposed model was not observed at 120 °C, indicating that the period in which SPP first forms, while conversion to intergrown crystals remains low, was too short to be captured with this sampling resolution.

3.2 Increasing the Rate of SPP Nucleation and Growth

The time to high conversion to SPP at 48 h is not as rapid as the synthesis of most aluminosilicate zeolites and silicalite-1. In order to facilitate large-scale production of this zeolite morphology for industrial application, a reduced hydrothermal synthesis time is highly desirable. To this end, we attempted to reduce the crystallization time by evaporation of co-solvent ethanol from the SPP sols prior to hydrothermal treatment. The addition of ethanol has been shown to slow down crystal growth of MFI [49–51], while the evaporation of ethanol can significantly decrease the time to crystallization [51]. Ethanol in precursor sols can also affect particle morphology and size distributions [52, 53]. Ethanol evaporation at a variety of stages in the preparation of SPP was attempted, with evaporation after the first room-temperature hydrolysis step demonstrating the best combination of good end morphologies and ease of sample processing of the denser gels. Evaporation was achieved rapidly, in about 3 min, as measured by mass difference for sols heated to 60 °C with stirring and headspace pressure decreased to just above the boiling point (results not shown). Sols were transparent following evaporation but with a significant increase in viscosity. They were then subjected to hydrothermal treatment at 115 °C for increasing amounts of time. Figure 5a and b show the resultant SAXS patterns and PDDF for a kinetic study of nucleation and growth of SPP with reduced ethanol content. There is a significant difference in appearance of the SAXS patterns between samples with or without ethanol co-solvent, and careful IFT analysis reveals this to be attributable to structure factor effects in the sol. The PDDF of all samples show oscillations in scattering lengths with period corresponding to the diameter of the precursor nanoparticles, indicating a structured dense gel of nanoparticles. Unlike samples with ethanol co-solvent, these oscillations due to structure factor are observed throughout all phases of hydrothermal synthesis in this denser system. A shift from Phase 1 to Phase 2 of growth between 3 and 6 h of hydrothermal treatment at 115 °C is less demarcated compared with ethanol-containing sols, but the low-angle scattering transition between Phase 2 and 3 is pronounced at 12 h. PDDF at this transition indicate a doubling in the largest scattering lengths, from 25 to 50 nm, along with a great increase in the density of these lengths, which is known to correspond to first appearance of crystals with SPP morphology. Similar to ethanol-containing sols at 120 °C, sols without ethanol seem to quickly bypass Phase 3a and continually consume the precursor amorphous particle population from 12–24 h, which is evident in the decrease of scattering intensity of the shoulders at $q = 2$ and 3/nm. After 30 h, SAXS profiles with a much different low-angle behavior are observed. Corresponding PDDF indicate that scattering lengths less than 20 nm become more common in the sol, and the structure factor effect resulting from the dense precursor nanoparticle gel becomes weaker. TEM images of sols at Phase 3b (Fig. 5c) after washing by centrifugation reveal the crystals to be of the SPP morphology, but most of the pentasil zeolite sheets are not intersecting at right angles indicating damage by sonication (used to disperse particles before TEM sample preparation) due to the low frequency of branching. With higher conversion after 36 h of hydrothermal treatment (Fig. 5d), the intergrowth becomes more regular and at right-angles. Argon adsorption isotherms (Fig. S4, Supplementary Information) show an increase in gas uptake with increasing pressure and desorption hysteresis, indicating that the samples are mesoporous. NLDFT modeling of cumulative gas uptake as a function of pore diameter, and its derivative dV(log d), for collected isotherms confirm the high mesoporosity for samples in both Phase 2 and Phase 3b between

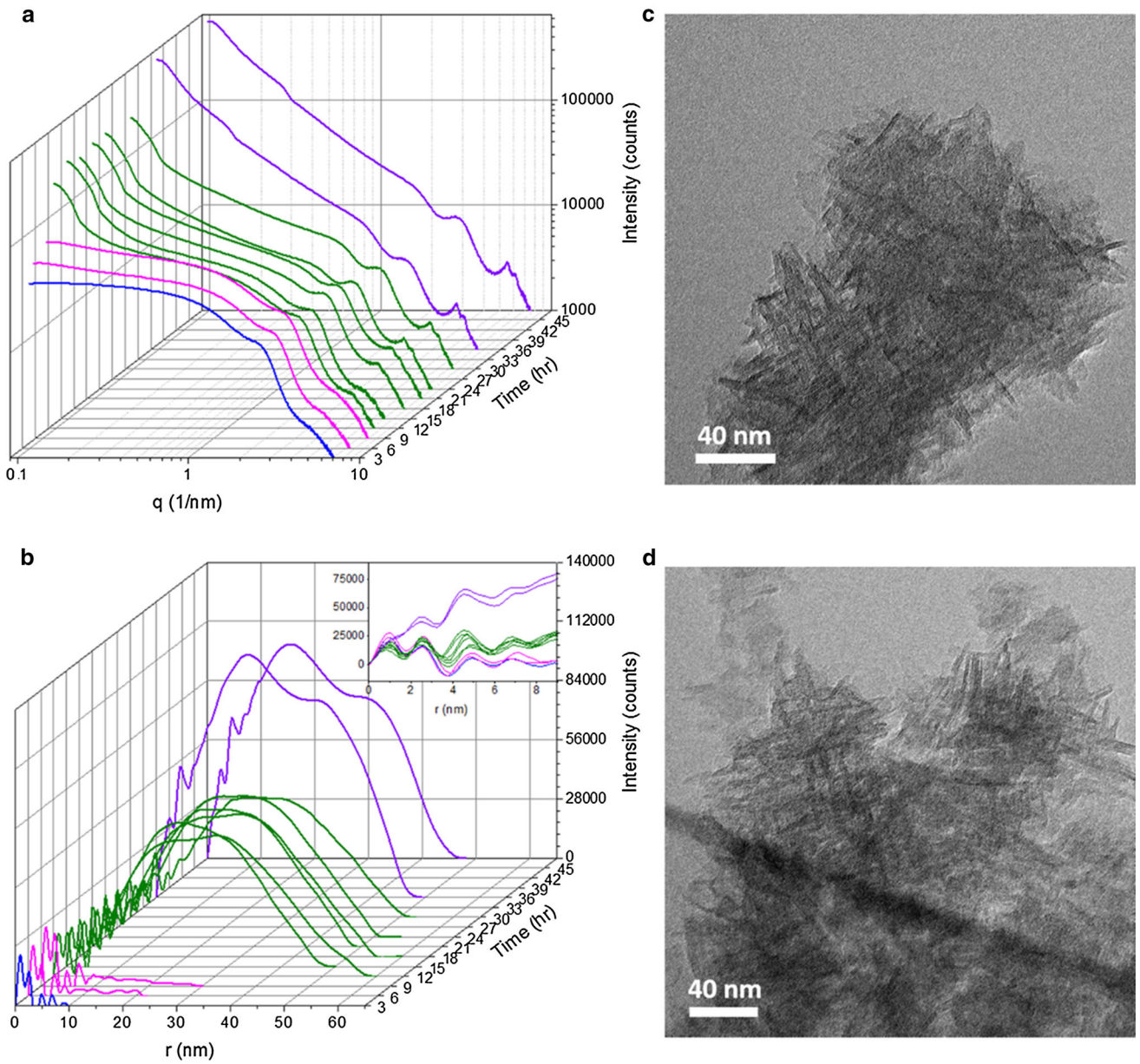

Fig. 5 SAXS patterns (**a**) and corresponding PDDF (**b**) from SPP sols with estimated composition 10 SiO_2:3 TBPOH:100 H_2O:2 EtOH after 3, 6, 9, 12, 15, 18, 21, 24, 30, 36, and 48 h of hydrothermal synthesis time at 115 °C. *Blue*, hydrothermal Phase 1 of growth; *magenta*, hydrothermal Phase 2; *green*, hydrothermal Phase 3a; *purple*, hydrothermal Phase 3b. *Inset* shows highlight overlay of PDDF in the region from 0–10 nm. TEM images of sols washed by centrifugation after 12 h (**c**) and 48 h (**d**) of hydrothermal synthesis

1 and 10 nm. There is also no significant difference between low-pressure isotherm regions between SPP prepared with or without ethanol evaporation, indicating that framework crystallinity is unchanged—a result further confirmed by XRD patterns of the materials (Fig. S5, Supplementary Information). In summary, ethanol evaporation from sols after hydrolysis leads to SPP crystal formation in 12 h, less than half the time of samples containing ethanol. Though XRD and Ar adsorption data suggest there is little difference between SPP crystals synthesized with or without the presence of ethanol, TEM suggests that the SPP morphologies obtained with ethanol removal are not as well defined (i.e., consisting of well-developed orthogonally intergrown layers) as the ones obtained in the presence of ethanol. Depending on the quality of morphology required for applications, ethanol evaporation is a promising technique for reducing the synthesis time and increasing throughput.

3.3 Optimization of SPP Intergrowth Morphology

SPP sols with composition 10 SiO_2:3 TBPOH:x MOH:100 H_2O:40 EtOH, were M is either K or Na and x ranges from 0 to 0.5, were crystallized at 115 °C to investigate the effect of alkali metal cation on morphology. To assess the crystallinity of the particles, XRD patterns were collected from the as-synthesized and calcined samples with varying additions of sodium to the synthesis sol (Fig. 6). Following calcination, peaks in the range 0° to 25° 2θ increase in intensity, possibly due to the further condensation and increasing crystallinity of the particles. With increasing NaOH, the width of XRD peaks in the range 15° to 25° 2θ improves. There is no evidence for the (110) and (330) peaks in the patterns with increasing sodium content, peaks which exist in MEL and are prohibited in the MFI structure

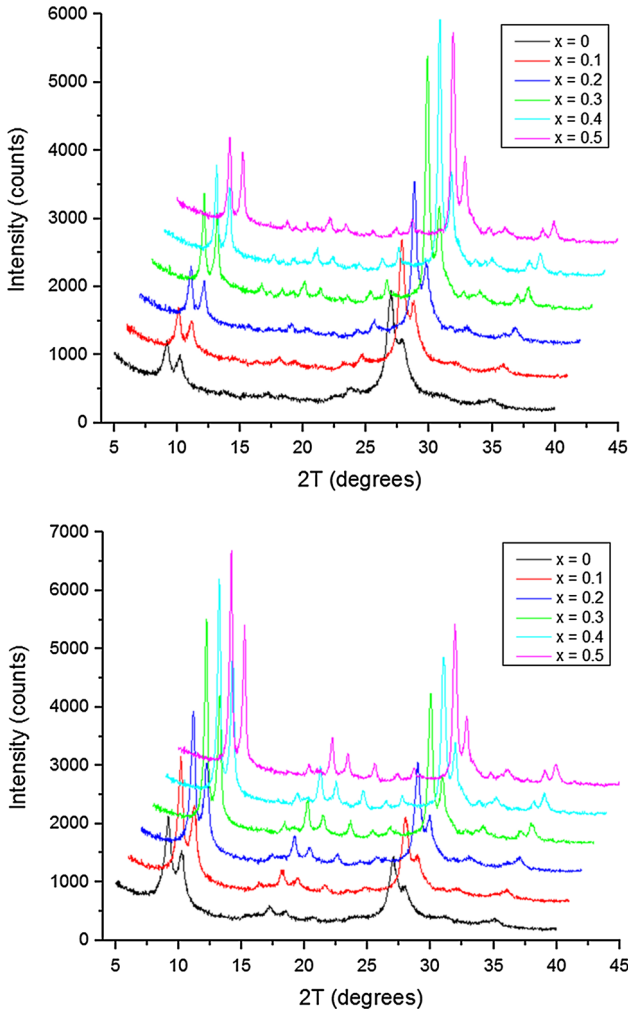

Fig. 6 X-ray diffraction patterns of as-synthesized (*top*) and calcined (*bottom*) SPP materials crystallized from sols with composition 10 SiO_2:3 TBPOH:xNaOH:100 H_2O:40 EtOH. *Black*, x = 0; *red*, x = 0.1; *blue*, x = 0.2; *green*, x = 0.3; *cyan*, x = 0.4; *magenta*, x = 0.5

[54]. The (10 0 0) peak splitting due to symmetry breaking in MFI has previously been used to identify fractions of phases in large MFI/MEL crystals [55, 56]. However, due to significant peak broadening in the collected patterns from these small crystals, such analysis cannot be performed accurately. To observe the morphology of the particles, TEM images were taken of crystals formed from sols with added Na in the range x = 0–0.5 (Fig. 7). When no NaOH is added, smaller crystals were obtained, comprised of nanosheets, which are relatively stunted. With x = 0.1 or 0.2, particles have a better defined overall square periphery and are primarily composed of single-unit cell thick nanosheets along the b-axis, and well developed in the other dimensions (as indicated by the sharper image contrast) intergrown at right angles. However, when the addition of NaOH to the sol reaches x = 0.3, a sharp transition occurs in the morphology of the resulting crystals (Fig. 7d). Denser zeolite with prolate ellipsoid shape forms that appears to be composed of domains with much larger than unit cell thickness. The trend towards densification continues as x is increased to 0.4 and then 0.5, at which point single-crystals of prolate shape and with no mesoporosity can be observed via continuous lattice fringes throughout the crystal (Fig. S6, Supplementary Information). High-resolution TEM (HRTEM) imaging was also conducted on (001) oriented particles to carefully inspect the crystal structure and morphology obtained in the presence of Na. Figure 8 shows (001)-oriented particles from SPP synthesis with x = 0.1, and 0.2 in the synthesis sol. With Si/M = 100, well-defined SPP morphology was obtained i.e., well-developed MFI nanosheets along a- and c-axis with single unit cell thickness along the b-axis intergrown at right angles comprise the majority of the particle volume. Upon increase of the cation content to Si/M = 50, widening of the zeolite nanosheets along the b-axis is observed.

This densification upon increase of sodium can be observed with argon adsorption. Linear plots of isotherms shown in Fig. 9a demonstrate that with increasing sodium content, gas uptake is decreased in the mesopore adsorption region from P/P_o = 0.1–0.8. The hysteresis observed and total gas adsorption for x = 0.1 and 0.2 is most similar to published Ar adsorption data from Zhang et al., which agrees with TEM data that these samples are closest to the morphologies reported in that previous study [27]. In the micropore adsorption region below 0.01 P/P_o expanded in view in Fig. 9b, samples with x = 0 and 0.1 both are coincident with published adsorption isotherms of SPP from Zhang et al., and micropore adsorption increases with increasing sodium content. This increased adsorption is due to widening of the MFI nanosheets, which results in more internal microporosity per unit mass of the material [15]. From NLDFT modeling of cumulative gas uptake vs. pore

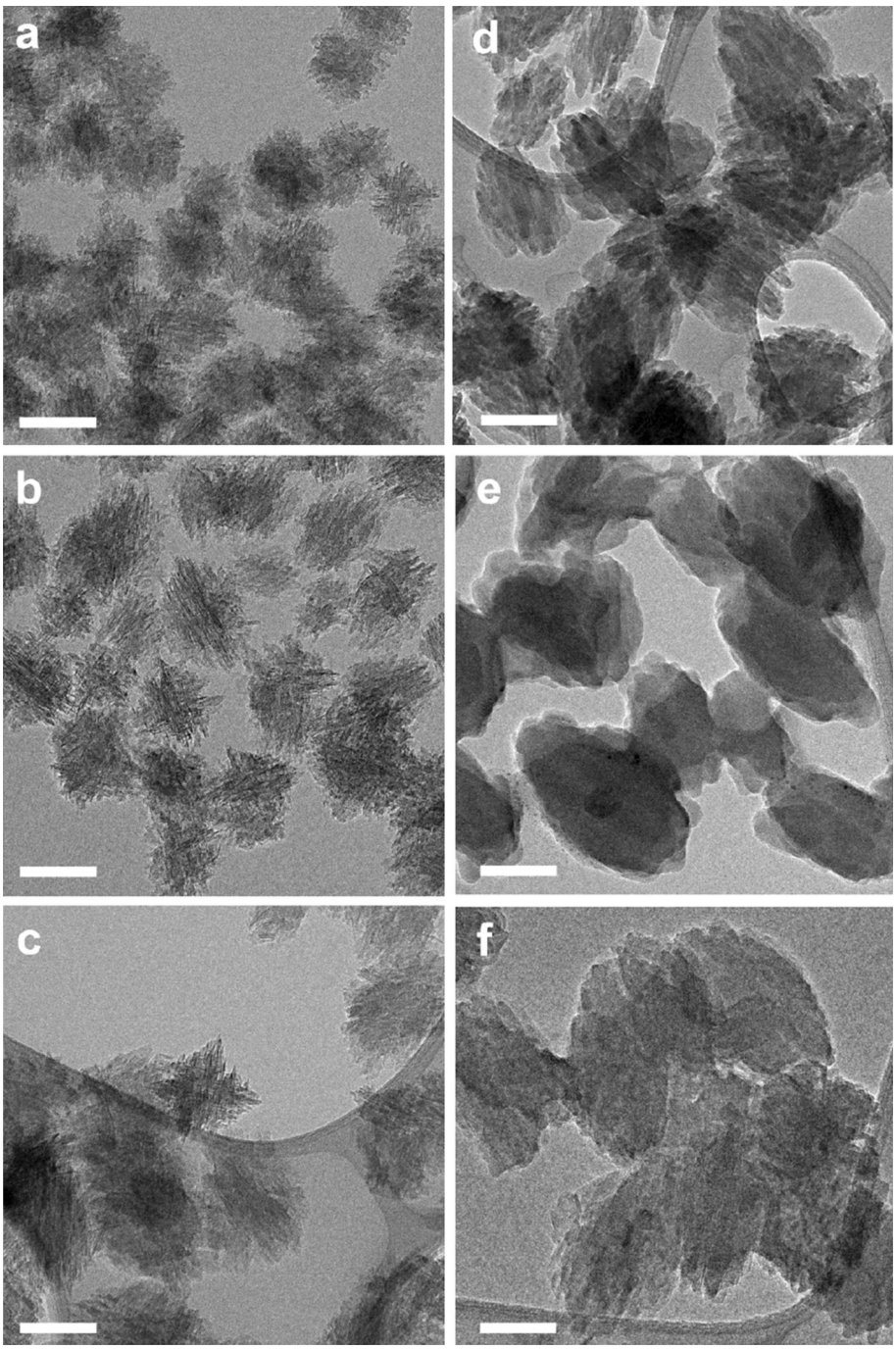

Fig. 7 TEM images of as-synthesized SPP materials crystallized from sols with composition 10 SiO_2:3 TBPOH:xNaOH:100 H_2O:40 EtOH. **a** x = 0; **b** x = 0.1; **c** x = 0.2; **d** x = 0.3; **e** x = 0.4; **f** x = 0.5. *Scale bar* 100 nm

size (Fig. 9c) and its derivative (Fig. 9d), it can be seen that at x = 0.5, mesoporosity is as low as commercial ZSM-5, agreeing with the TEM observation that densification of the crystals is complete and non-mesoporous zeolite crystals are obtained. The prolate spheroidal shape of these crystals at high sodium content is similar to ZSM-5/ZSM-11 intergrowths synthesized using tetrabutylammonium hydroxide as the structure directing agent with Si/cation ratio of 42 [57]. The particles resulting from increased sodium addition are likely also a dense intergrowth of MFI and MEL.

Samples were also synthesized with addition of KOH to see if the alkali metal cation effect on morphology was specific to sodium. Figure 10 shows TEM images of SPP formed with increasing amounts of KOH added to the synthesis sol. From the images, it appears that the effect is similar. Due to the small crystal size and associated peak broadening, the differences in morphological quality

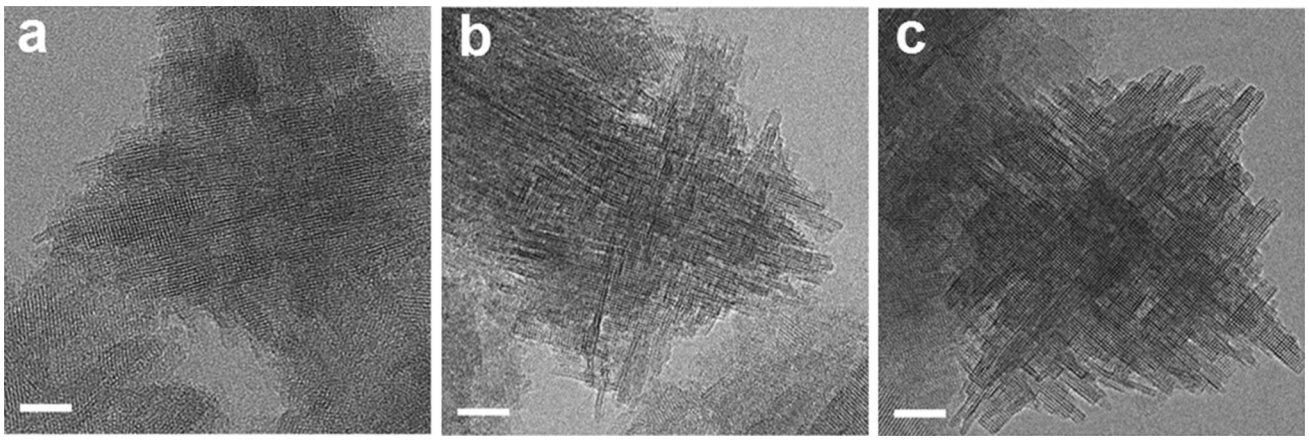

Fig. 8 HRTEM images of as-synthesized SPP materials crystallized from sols with composition 10 SiO_2:3 TBPOH:xNaOH:100 H_2O:40 EtOH. **a** x = 0; **b** x = 0.1; **c** x = 0.2. *Scale bar* 20 nm

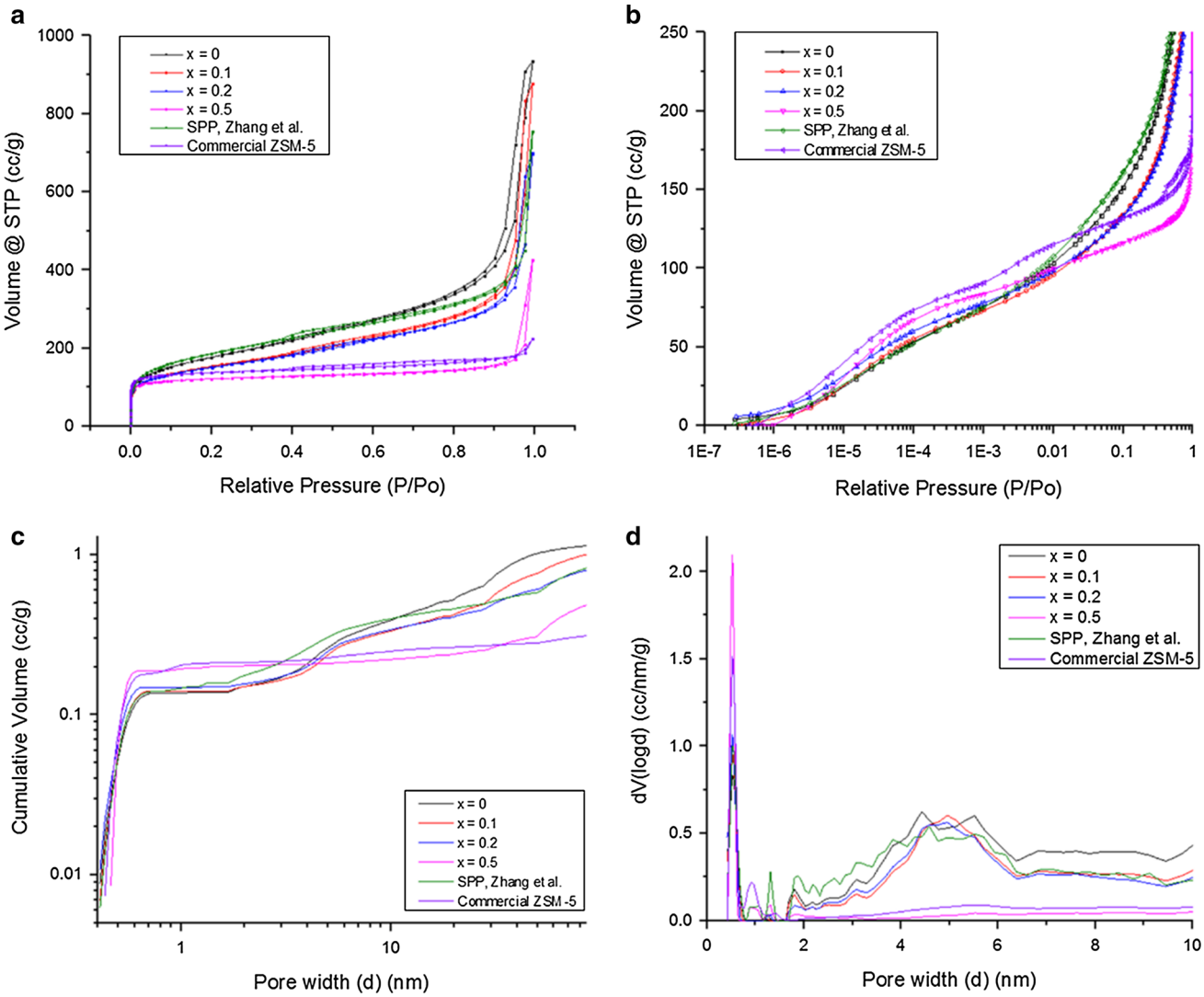

Fig. 9 Argon adsorption/desorption isotherms plotted on linear (**a**) and semi-log (**b**) scales for calcined SPP materials crystallized from sols with composition 10 SiO_2:3 TBPOH:xNaOH:100 H_2O:40 EtOH. NLDFT modeling results of isotherm adsorption branch for cumulative pore volume (**c**) and differential pore volume dV(log d) (**d**) as a function of pore width. *Black*, x = 0; *red*, x = 0.1; *blue*, x = 0.2, *magenta*, x = 0.5; *green*, SPP from Zhang et al.; *purple*, commercial ZSM-5 from Zhang et al. [27]

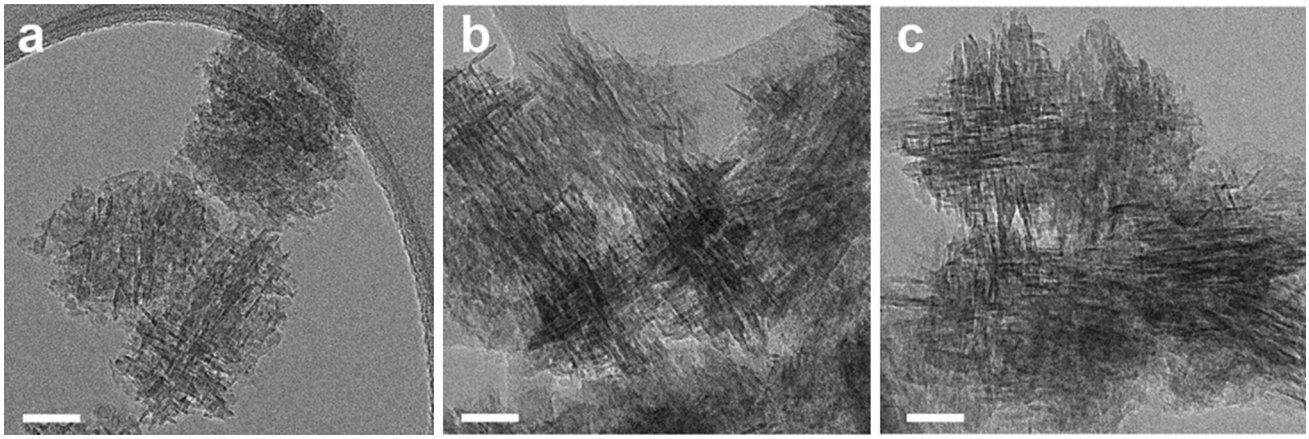

Fig. 10 TEM images of calcined SPP materials crystallized from sols with composition 10 SiO_2:3 TBPOH:xKOH:100 H_2O:40 EtOH. **a** x = 0.1; **b** x = 0.2; **c** x = 0.3. *Scale bar* 40 nm

cannot be distinguished by X-ray diffraction (XRD), where all of the samples are undifferentiated from previously-published SPP patterns (Fig. S7 Supplementary Information). To investigate if the morphological change was due to the presence of sodium or potassium and not due to increased pH, samples with additional TBPOH were synthesized under the same conditions. Argon adsorption (Fig. S8, Supplementary Information) and XRD (Fig. S9, Supplementary Information) results indicated that sols with composition 10 SiO_2:3 TBPOH:0NaOH:100 H_2O:40 EtOH and 10: 4: 0: 100: 40 yielded samples of the same morphology, as was previously reported by Zhang et al. [27]. Addition of twice as much base as the highest additional amount in the NaOH sample series did not lead to the dense morphology, so the effect is tentatively attributed to the presence of Na and K cations.

4 Conclusions

The formation process of SPP zeolite exhibits dynamic features similar to the silicalite-1 system, such as two precursor nanoparticle populations of size 2 and 6 nm, which evolve upon TEOS hydrolysis and low-temperature heating, respectively. After 24 h of heating at the hydrothermal synthesis temperature of 115 °C, single-unit cell thick plates of MFI nucleate in the sol. The sudden emergence of larger crystalline nanoparticles with SPP morphology occurs after 30 h of heating, followed by the decline of precursor nanoparticles populations and increase in SPP crystal density after 40 h. SAXS is able to capture sizing information about these three nanoparticle populations and qualitatively assess their relative proportions simultaneously, while TEM can confirm the size and provide morphology and crystallinity information unavailable from SAXS at early stages of nucleation.

SPP materials comprised of orthogonally-intergrown MFI nanosheets that are well-developed along a- and c-axes and of single-unit cell thickness along b-axis throughout large nanoparticles were previously difficult to produce robustly. The addition of Na or K cations to the synthesis sol in the range of Si/M = 50–100 leads to robust crystallization of such well-defined SPP. Addition of cations at higher concentrations leads to widening of nanosheets, suggesting that this is due to increased fraction of MFI phase in the intergrowths. Removal of ethanol is found to accelerate growth, but the SPP obtained is not as well-defined as in the presence of ethanol.

Acknowledgments This article was based on work supported as part of the Catalysis Center for Energy Innovation (CCEI), an Energy Frontier Research Center (EFRC) funded by the U.S. Department of Energy, Office of Science, Office of Basic Energy Sciences under Award No. DE-SC0001004. Partial support was provided by the Petroleum Institute, Abu Dhabi, UAE.

References

1. Burkett SL, Davis ME (1994) Mechanism of structure direction in the synthesis of Si-ZSM-5: an investigation by intermolecular 1H–29Si CP MAS NMR. J Phys Chem 98:4647–4653
2. Burkett SL, Davis ME (1995) Mechanism of structure direction in the synthesis of pure-silica zeolites. 2. Hydrophobic hydration and structural specificity. Chem Mater 7:1453–1463
3. Burkett SL, Davis ME (1995) Mechanisms of structure direction in the synthesis of pure-silica zeolites. 1. Synthesis of TPA/Si-ZSM-5. Chem Mater 7:920–928
4. Tsapatsis M, Lovallo M, Okubo T et al (1995) Characterization of zeolite L nanoclusters. Chem Mater 7:1734–1741. doi:10.1021/cm00057a025
5. Tsapatsis M, Lovallo M, Davis ME (1996) High-resolution electron microscopy study on the growth of zeolite L nanoclusters. Microporous Mater 5:381–388. doi:10.1016/0927-6513(95)00069-0

6. Beck LW, Davis ME (1998) Alkylammonium polycations as structure-directing agents in MFI zeolite synthesis. Microporous Mesoporous Mater 22:107–114. doi:10.1016/S1387-1811(98)00096-1
7. Tsapatsis M (2014) 2-Dimensional zeolites. AIChE J 60:2374–2381. doi:10.1002/aic
8. Pérez-Ramírez J, Christensen CH, Egeblad K et al (2008) Hierarchical zeolites: enhanced utilisation of microporous crystals in catalysis by advances in materials design. Chem Soc Rev 37:2530–2542. doi:10.1039/b809030k
9. Davis ME (1991) Zeolites and molecular sieves: not just ordinary catalysts. Ind Eng Chem Res 30:1675–1683
10. Davis ME, Lobo RF (1992) Zeolite and molecular sieve synthesis. Chem Mater 4:756–768
11. Davis ME (2002) Ordered porous materials for emerging applications. Nature 417:813–821
12. Serrano DP, Escola JM, Pizarro P (2013) Synthesis strategies in the search for hierarchical zeolites. Chem Soc Rev 42:4004–4035. doi:10.1039/c2cs35330j
13. Zečević J, de Jong KP (2013) Architecture at the nanoscale-self-pillared zeolite nanosheets. ChemCatChem 5:417–418. doi:10.1002/cctc.201200596
14. Möller K, Bein T (2013) Mesoporosity—a new dimension for zeolites. Chem Soc Rev 42:3689–3707. doi:10.1039/c3cs35488a
15. Bai P, Olson DH, Tsapatsis M, Siepmann JI (2014) Understanding the unusual adsorption behavior in hierarchical zeolite nanosheets. ChemPhysChem 15:2225–2229. doi:10.1002/cphc.201402189
16. Chang C, Teixeira A, Li C et al (2013) Enhanced molecular transport in hierarchical silicalite-1. Langmuir 29:13943–13950
17. Wang J, Yue W, Zhou W, Coppens M-O (2009) TUD-C: a tunable, hierarchically structured mesoporous zeolite composite. Microporous Mesoporous Mater 120:19–28. doi:10.1016/j.micromeso.2008.08.060
18. Choi M, Na K, Kim J et al (2009) SI: stable single-unit-cell nanosheets of zeolite MFI as active and long-lived catalysts. Nature 461:246–249. doi:10.1038/nature08288
19. Fan W, Snyder MA, Kumar S et al (2008) Hierarchical nanofabrication of microporous crystals with ordered mesoporosity. Nat Mater 7:984–991. doi:10.1038/nmat2302
20. Lee P-S, Zhang X, Stoeger JA et al (2011) Sub-40 nm zeolite suspensions via disassembly of three-dimensionally ordered mesoporous-imprinted silicalite-1. J Am Chem Soc 133:493–502
21. Chen H, Wydra J, Zhang X et al (2011) Hydrothermal synthesis of zeolites with three-dimensionally ordered mesoporous-imprinted structure. J Am Chem Soc 133:12390–12393. doi:10.1021/ja2046815
22. Na K, Choi M, Park W et al (2010) Pillared MFI zeolite nanosheets of a single-unit-cell thickness. J Am Chem Soc 132:4169–4177. doi:10.1021/ja908382n
23. Groen JC, Zhu W, Brouwer S et al (2007) Direct demonstration of enhanced diffusion in mesoporous ZSM-5 zeolite obtained via controlled desilication. J Am Chem Soc 129:355–360. doi:10.1021/ja065737o
24. Groen JC, Moulijn JA, Pérez-Ramírez J (2006) Desilication: on the controlled generation of mesoporosity in MFI zeolites. J Mater Chem 16:2121. doi:10.1039/b517510k
25. Müller M, Harvey G, Prins R (2000) Comparison of the dealumination of zeolites beta, mordenite, ZSM-5 and ferrierite by thermal treatment, leaching with oxalic acid and treatment with $SiCl_4$. Microporous Mesoporous Mater 34:135–147
26. Van Donk S, Janssen AH, Bitter JH, de Jong KP (2003) Generation, characterization, and impact of mesopores in zeolite catalysts. Catal Rev 45:297–319. doi:10.1081/CR-120023908
27. Zhang X, Liu D, Xu D et al (2012) Synthesis of self-pillared zeolite nanosheets by repetitive branching. Science 336:1684–1687. doi:10.1126/science.1221111
28. Chaikittisilp W, Suzuki Y, Mukti RR et al (2013) Formation of hierarchically organized zeolites by sequential intergrowth. Angew Chem 125:3439–3443. doi:10.1002/ange.201209638
29. Inayat A, Knoke I, Spiecker E, Schwieger W (2012) Assemblies of mesoporous FAU-type zeolite nanosheets. Angew Chem Int Ed Engl 51:1962–1965. doi:10.1002/anie.201105738
30. Khaleel M, Wagner AJ, Mkhoyan KA, Tsapatsis M (2014) On the rotational intergrowth of hierarchical FAU/EMT zeolites. Angew Chem Int Ed. doi:10.1002/anie.201402024
31. Jeong H-K, Krohn J, Sujaoti K, Tsapatsis M (2002) Oriented molecular sieve membranes by heteroepitaxial growth. J Am Chem Soc 124:12966–12968
32. Okubo T, Wakihara T, Plévert J et al (2001) Heteroepitaxial growth of a zeolite. Angew Chem Int Ed 40:1069–1071
33. Millward G, Ramdas S, Thomas J (1985) On the direct imaging of offretite, cancrinite, chabazite and other related ABC-6 zeolites and their intergrowths. Proc R Soc Lond A Math Phys Eng. Sci 399:57–71
34. Xu D, Swindlehurst GR, Wu H et al (2014) On the synthesis and adsorption properties of single-unit-cell hierarchical zeolites made by rotational intergrowths. Adv Funct Mater 24:201–208. doi:10.1002/adfm.201301975
35. Bergmann A, Fritz G, Glatter O (2000) Solving the generalized indirect Fourier transformation (GIFT) by Boltzmann simplex simulated annealing (BSSA). J Appl Crystallogr 33:1212–1216. doi:10.1107/S0021889800008372
36. Behr MJ, Mkhoyan KA, Aydil ES (2010) Orientation and morphological evolution of catalyst nanoparticles during carbon nanotube growth. ACS Nano 4:5087–5094. doi:10.1021/nn100944n
37. Ravikovitch PI, Neimark AV (2001) Characterization of nanoporous materials from adsorption and desorption isotherms. Colloids Surf A Physicochem Eng Asp 187–188:11–21
38. Rimer JD, Vlachos DG, Lobo RF (2005) Evolution of self-assembled silica- tetrapropylammonium nanoparticles at elevated temperatures. J Phys Chem B 109:12762–12771
39. Davis TM, Drews TO, Ramanan H et al (2006) Mechanistic principles of nanoparticle evolution to zeolite crystals. Nat Mater 5:400–408. doi:10.1038/nmat1636
40. Kumar S, Wang Z, Penn RL, Tsapatsis M (2008) A structural resolution cryo-TEM study of the early stages of MFI growth. J Am Chem Soc 130:17284–17286. doi:10.1021/ja8063167
41. Aerts A, Haouas M, Caremans T et al (2010) Investigation of the mechanism of colloidal silicalite-1 crystallization by using DLS, SAXS, and 29Si NMR spectroscopy. Chemistry 16:2764–2774. doi:10.1002/chem.200901688
42. Rimer JD, Fedeyko JM, Vlachos DG, Lobo RF (2006) Silica self-assembly and synthesis of microporous and mesoporous silicates. Chemistry 12:2926–2934. doi:10.1002/chem.200500684
43. Porod G (1982) General Theory. In: Glatter O, Kratky O (eds) Small-angle X-ray scatt, 1st edn. Academic Press, London, pp 17–51
44. Weyerich B, Brunner-Popela J, Glatter O (1999) Small-angle scattering of interacting particles. II. Generalized indirect Fourier transformation under consideration of the effective structure factor for polydisperse systems. J Appl Crystallogr 32:197–209. doi:10.1107/S0021889898011790
45. Mintova S, Olson NH, Senker J, Bein T (2002) Mechanism of the transformation of silica precursor solutions into Si-MFI zeolite. Angew Chem Int Ed Engl 41:2558–61
46. Petry DP, Haouas M, Wong SCC et al (2009) Connectivity analysis of the clear sol precursor of silicalite: are nanoparticles aggregated oligomers or silica particles? J Phys Chem C 113:20827–20836. doi:10.1021/jp906276g
47. Kumar S, Davis TM, Ramanan H et al (2007) Aggregative growth of silicalite-1. J Phys Chem B 111:3398–3403. doi:10.1021/jp0677445

48. Tokay B, Erdem-Şenatalar A (2012) Variation of particle size and its distribution during the synthesis of silicalite-1 nanocrystals. Microporous Mesoporous Mater 148:43–52. doi:10.1016/j.micromeso.2011.07.011
49. Cundy C, Lowe B, Sinclair D (1993) Crystallisation of zeolitic molecular sieves: direct measurements of the growth behaviour of single crystals as a function of synthesis conditions. Faraday Discuss 95:235–252
50. Persson A, Schoeman B, Sterte J, Otterstedt J (1994) The synthesis of discrete colloidal particles of TPA-silicalite-1. Zeolites 14:557–567
51. Cheng C-H, Shantz DF (2005) Silicalite-1 growth from clear solution: effect of alcohol identity and content on growth kinetics. J Phys Chem B 109:19116–19125. doi:10.1021/jp0524633
52. Huang Y, Yao J, Zhang X et al (2011) Role of ethanol in sodalite crystallization in an ethanol–Na_2O–Al_2O3–SiO_2–H_2O system. CrystEngComm 13:4714. doi:10.1039/c1ce05194f
53. Wang H, Wang Z, Huang L et al (2001) Surface patterned porous films by convection-assisted dynamic self-assembly of zeolite nanoparticles. Langmuir 17:2572–2574
54. Terasaki O, Ohsuna T, Sakuma H et al (1996) Direct observation of "pure MEL type" zeolite. Chem Mater 8:463–468
55. Jablonski G, Sand L, Gard J (1986) Synthesis and identification of ZSM-5/ZSM-11 pentasil intergrowth structures. Zeolites 6:396–402
56. Piccione PM, Davis ME (2001) A new structure-directing agent for the synthesis of pure-phase ZSM-11. Microporous Mesoporous Mater 49:163–169. doi:10.1016/S1387-1811(01)00414-0
57. Millward G, Ramdas S, Thomas J (1983) Evidence for semi-regularly ordered sequences of mirror and inversion symmetry planes in ZSM-5/ZSM-11 shape-selective zeolitic catalysts. J Chem Soc Faraday Trans 2(79):1075–1082